CHEMISTRY OF MATERIALS

ARTICLE

pubs.acs.org/cm

High-Temperature and High-Pressure Aqueous Solution Formation, Growth, Crystal Structure, and Magnetic Properties of $BiFeO_3$ Nanocrystals

Jian-Li Mi, Thomas N. Jensen, Mogens Christensen, Christoffer Tyrsted, Jens E. Jørgensen, and Bo B. Iversen*

Centre for Materials Crystallography, Department of Chemistry and iNANO, Aarhus University, Langelandsgade 140, DK-8000, Aarhus, Denmark

Supporting Information

ABSTRACT: In situ synchrotron radiation powder X-ray diffraction (SR-PXRD) was applied to study the formation and growth of $BiFeO_3$ nanocrystals, revealing that phase pure $BiFeO_3$ can be obtained in high-temperature, high-pressure aqueous solution using $Bi(NO_3)_3$ and $Fe(NO_3)_3 \cdot 9H_2O$ as precursors and KOH as mineralizer. The method gives a rapid way for preparation of nanomaterials, and the formation of $BiFeO_3$ can be finished within seconds after its initial nucleation in near-critical aqueous solution. As proof of concept $BiFeO_3$ nanocrystals were subsequently synthesized in a continuous flow supercritical system and for reference also in autoclaves. High resolution multitemperature SR-PXRD data were measured between 100 and 1000 K with a step size of 100 K. The magnetic properties of both the autoclave and the continuous flow samples are studied.

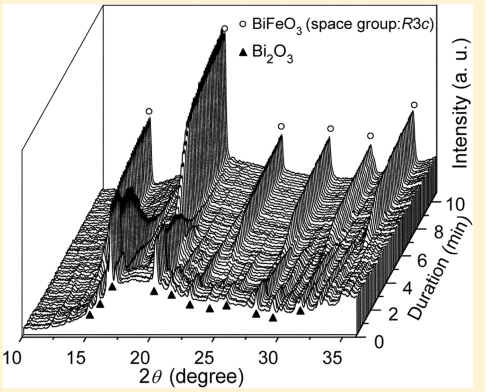

KEYWORDS: synchrotron radiation, supercritical synthesis, bismuth ferrite, magnetic properties

1. INTRODUCTION

Multiferroic materials, with electric and magnetic order parameters coupling in the same phase, have attracted a great deal of attention due to their potential applications in data storage, spintronics, sensors, quantum electromagnets, and electronics.[1−5] $BiFeO_3$ is one of the most widely studied multiferroic materials, primarily because both its electrical and magnetic ordering occur above room temperature. $BiFeO_3$ shows antiferromagnetic ordering with a reasonably high Néel temperature (∼643 K) and ferroelectric ordering with a high Curie temperature (∼1098 K).[6] In 2003, Ramesh and co-workers[1] reported that $BiFeO_3$ thin films have unexpectedly large remnant polarization, together with significant enhancement of magnetization compared with the bulk, and this stimulated the current interest in $BiFeO_3$. Normally, nanostructures exhibit distinctive size effects affecting physical properties such as magnetic and ferroelectric ordering which are of importance for applications in various nanoscale devices. Besides the intensive study of films, there is also a rapid growth of research in $BiFeO_3$ nanoparticles. This makes it desirable to find a facile way to prepare phase pure $BiFeO_3$ nanocrystals.

Several hydrothermal methods have been demonstrated for the preparation of $BiFeO_3$ particles.[7−10] There are, however, some problems associated with conventional hydrothermal methods, including the limited control of temperature and pressure as well as the slow heating rate. Synthesis in high temperature and high pressure solutions, that is, supercritical or near-critical solutions, is a promising way for controlling synthesis conditions and manipulating the size and size distribution of nanoparticles. Supercritical fluids exhibit particularly attractive properties such as gas-like transport properties in diffusivity, viscosity, and surface tension, while maintaining liquid-like properties such as high-solvation capability and high density. These unique properties make supercritical fluids attractive solvents in chemical processes. Over the past decade supercritical fluid synthesis has been used extensively to prepare a wide range of nanomaterials.[11−13] Supercritical fluid reactions can be carried out in different types of reactors.[13] In a continuous flow supercritical system, the solvent is first pressurized and heated to the desired temperature. The pressurized reactants meet the solvent at the mixing point, leading to rapid heating of the reactants and immediate reaction. In general, very little is known about the chemical reactions taking place during nanoparticle formation from solutions at high temperature and high pressure. Recently, direct studies of nanocrystal growth processes were

Received: September 8, 2010
Revised: December 28, 2010
Published: January 20, 2011

ACS Publications © 2011 American Chemical Society

obtained through the use of synchrotron radiation and a specially designed in situ reactor, capable of withstanding the extreme supercritical conditions, while simultaneously allowing X-ray penetration.[14−18]

In this study, we use high-temperature, high-pressure aqueous solutions of metal salts to prepare $BiFeO_3$ nanocrystals. In situ synchrotron radiation powder X-ray diffraction (SR-PXRD) was applied to study the formation and grain growth of the $BiFeO_3$ particles. Subsequently, $BiFeO_3$ nanoparticles were successfully synthesized in a continuous flow supercritical system, and for comparison nanocrystals were also prepared in an autoclave. High resolution multitemperature SR-PXRD studies as well as magnetic property measurements were used for the characterization of the $BiFeO_3$ nanoparticles.

2. EXPERIMENTAL DETAILS

2.1. In Situ Synchrotron Radiation Experiments. Formation and growth of the $BiFeO_3$ nanocrystals was studied by in situ SR-PXRD. All chemical reagents used in the experiments were analytical grade. For the preparation of the precursor, stoichiometric amounts of $Fe(NO_3)_3 \cdot 9H_2O$ and $Bi(NO_3)_3 \cdot 5H_2O$ were added in 4 M KOH solution. The mixture was ultrasonically dispersed for 10 min, and the solution was injected into a sapphire capillary. After injection, the sapphire capillary was sealed, pressurized, and subsequently heated to the targeted temperature using a HPLC pump and a hot air blower, respectively.[19] Experiments at different reaction temperatures of 160, 200, 250, and 350 °C were performed at a pressure of 250 bar. The in situ synchrotron data were measured at beamline I711, at MAX-lab, Sweden, using a custom designed sample stage and a Mar 165 CCD detector. The monochromator delivered a beam with a wavelength of 0.9496 Å, and the time resolution was 11.35 s between each frame, of which 7.35 s was detector dead time due to readout. The obtained powder diffraction patterns were integrated using FIT2D and Rietveld refined using the Fullprof program.[20] Data were also collected on a LaB_6 standard to correct for instrumental broadening in the refinements. For convenience, the samples in the in situ study are named as "IS*x*", where "IS" denotes the in situ study and "*x*" the synthesis temperature.

2.2. Synthesis in a Continuous Flow Supercritical Reactor and in an Autoclave. For the continuous flow synthesis in supercritical media, our group has built up a specialized synthesis apparatus that is capable of handling high temperature and high pressure.[11] For the typical continuous flow supercritical synthesis of $BiFeO_3$, the precursors were prepared by dissolving stoichiometric amounts of $Fe(NO_3)_3 \cdot 9H_2O$ and $Bi(NO_3)_3 \cdot 5H_2O$ in 0.4 M HNO_3. A solution of KOH with concentration of 2 M was used as the supercritical medium. The synthesis was done above the critical point of water at temperature and pressure of 400 °C and 250 bar, respectively. The flow rates of the precursor and the solvent were both adjusted to 10 mL/min. The sample is named as "BFO_SC" for convenience, where "SC" denotes the supercritical synthesis in the continuous flow system.

Conventional hydrothermal synthesis of $BiFeO_3$ in an autoclave was performed for comparison with the supercritical synthesis. In a typical synthesis, stoichiometric amounts of $Fe(NO_3)_3 \cdot 9H_2O$ and $Bi(NO_3)_3 \cdot 5H_2O$ were added to a 4 M KOH solution. The mixture was ultransonically dispersed for 10 min and then transferred into a Teflon lined autoclave. The autoclave was heated and maintained at 180 °C for 6 h, followed by cooling in air to room temperature. The products were washed with distilled water and collected by centrifugation. The sample prepared by the hydrothermal method is named "BFO_H", where "H" denotes hydrothermal synthesis in an autoclave.

2.3. Characterizations and Magnetic Properties Measurements. The products from the supercritical synthesis and the hydrothermal synthesis were investigated using powder X-ray diffraction (PXRD) collected on a STOE powder diffractometer using Cu $K\alpha_1$ radiation (λ = 1.5406 Å). The morphology of the products was observed on NOVA600 field-emission scanning electron microscope (SEM) and Philips CM20 transmission electron microscope (TEM). Differential scanning calorimetry (DSC) measurements were done with a NETZSCH STA 449 thermoanalyzer in helium atmosphere with a heating rate of 10 K/h. Magnetic properties were characterized using the magnetic susceptibility option in a Quantum Design Physical Property Measurement System (PPMS). The temperature dependence of the magnetization was measured in a field of 1000 Oe after zero field cooling (ZFC) and field cooling (FC) in the temperature range from 2 to 300 K. The field dependence of the magnetization was measured at 10 and 300 K in fields from −5 to 5 T. Sample BFO_H was investigated by high resolution SR-PXRD between 100 and 1000 K in steps of 100 K. The multitemperature SR-PXRD data were collected at BL2B02 at SPring-8, Japan.[21] The wavelength (λ = 0.433089 Å) was determined from data measured on a CeO_2 standard. Rietveld refinements were carried out with the Fullprof program using a pseudo-Voigt profile function and a background modeled with linear interpolation.

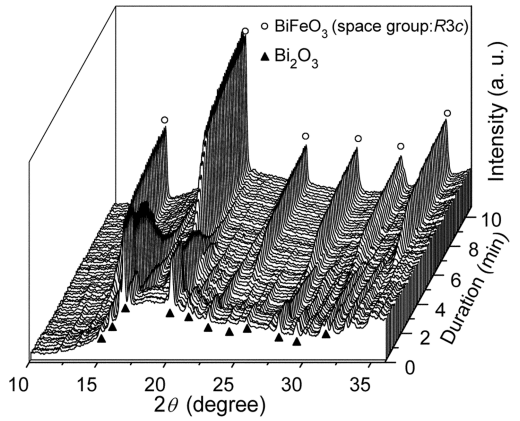

Figure 1. Time evolution of the in situ SR-PXRD patterns for the synthesis of sample IS200 in the reaction temperature of 200 °C.

3. RESULTS AND DISCUSSION

3.1. In Situ Study of Formation and Growth of $BiFeO_3$. The formation and growth of samples IS160, IS200, IS250, and IS300, which are performed at the temperatures of 160, 200, 250, and 350 °C, respectively, is in situ studied by SR-PXRD. Figure 1 shows the time evolution of the SR-PXRD patterns for the sample IS200 in the period from the starting of the recording time to about 11 min. The recording time started before the reactor was heated. Patterns were recorded for 1 min at room temperature, the heater was then turned on, and the reactor was heated to the desired temperature in approximately 15 s. The SR-PXRD patterns of the first 4 min reveal well-crystalline single phase Bi_2O_3 precipitates. All peaks can be indexed to the Bi_2O_3 phase with monoclinic space group $P2_1/c$. Iron may exist as a hydroxide with an amorphous structure in the reactor tube. The powder diffraction patterns as function of time show a decrease in Bi_2O_3 content, whereas the $BiFeO_3$ phase starts appearing after 4 min of reaction. Single phase $BiFeO_3$ is achieved at about 8 min. Other reaction conditions show similar processes, but the formation of $BiFeO_3$ occurs much earlier and more quickly when the reaction temperature increases. The time evolutions of SR-PXRD patterns for the samples IS160, IS250, and IS350 are available in the Supporting Information. Single phase $BiFeO_3$ is achieved at about 20, 3, and 2 min for IS160, IS250, and IS350,

dx.doi.org/10.1021/cm102575w |*Chem. Mater.* 2011, 23, 1158–1165

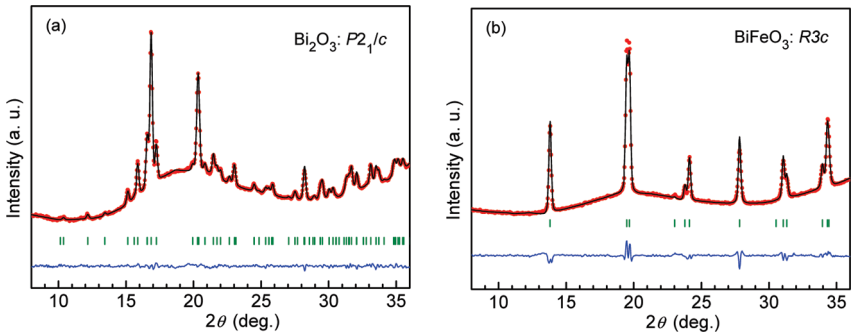

Figure 2. Typical refinement SR-PXRD patterns with observed, calculated, and difference patterns of Bi_2O_3 (a) and $BiFeO_3$ (b), corresponding to the reaction times of 2 and 20 min of sample IS200, respectively.

respectively. The formation of $BiFeO_3$ in the high-temperature, high pressure aqueous solution possibly involves the combination of crystalline bismuth oxide and amorphous ferric hydroxide.

The analysis of the formation rate and particle growth of $BiFeO_3$ was carried out using sequential Rietveld refinements in Fullprof. The background was modeled using linear interpolation with 22 points, and the particle size was refined from the peak broadening. A LaB_6 standard was used to correct for instrumental broadening in the refinements. The particle shape can be modeled using the spherical harmonic functions, and the peak broadening in different crystallographic directions can be described by[16]

$$\beta(\Theta,\Phi) = \frac{K\lambda}{\langle D(\Theta,\Phi)\rangle \cos(\theta)} = \frac{K\lambda}{\cos(\theta)} \sum A_{nml} Y_{nml}(\Theta,\Phi) \quad (1)$$

where A_{nml} are the refinable coefficients (i.e., the peak shape parameters) and Y_{nml} are the spherical harmonic functions. The refined coefficients, A_{nml}, were used to calculate the volume-weighted particle size. Figure 2a,b shows the typical refinement SR-PXRD patterns with observed, calculated, and difference patterns of Bi_2O_3 and $BiFeO_3$ for sample IS200 at the time of 2 and 20 min, respectively, and there is good agreement between the calculated patterns and the observed data. Table 1 displays the Rietveld refinement parameters corresponding to the two plots in Figure 2.

Figure 3a shows the time evolution of particle sizes of Bi_2O_3 and $BiFeO_3$ for sample IS200. The calculated particle size of Bi_2O_3 increases from 80 nm up to several hundred nanometers. Although the size of the Bi_2O_3 particles is too large to be reliably estimated, the trend of the particle size indicates growth of Bi_2O_3 upon heating. The Bi_2O_3 particles grew very fast as soon as the heating was turned on after 1 min. After initial formation, the crystallites of $BiFeO_3$ grow slowly up to an equilibrium size of about 40 nm. The amounts of Bi_2O_3 and $BiFeO_3$ are reflected by the scale factors as shown in Figure 3b. After 3 min the amount of Bi_2O_3 decreases, and then nucleation of $BiFeO_3$ is observed. The amount of $BiFeO_3$ quickly increases after the initial nucleation. The formation rate calculated by differentiating the scale factor is shown by the solid line in Figure 3b, which gives further details on the process. The formation rate is negative for Bi_2O_3 indicating that Bi_2O_3 is dissolved in the solution even though the grains of Bi_2O_3 are still growing. The formation of $BiFeO_3$ is very quick after its initial nucleation, and the formation rate becomes almost zero after 7 min of reaction indicating that the nucleation has ceased while the grain growth through Oswald ripening continues for a much longer duration.

Table 1. Refined Parameters in the Rietveld Analysis of the Bi_2O_3 and $BiFeO_3$ Phases Based on the in Situ SR-PXRD Data Shown in Figure 2[a]

formula	Bi_2O_3	$BiFeO_3$
space group	$P2_1/c$	$R3c$
no. of data points	1459	1459
no. of refined parameters	30	27
no. of reflections	300	32
R_P (%)	10.3	14.2
R_{WP} (%)	6.57	10.0
R_I (%)	6.01	5.11
R_F (%)	6.30	3.48
cell parameter a (Å)	5.8300(5)	5.5569(1)
cell parameter b (Å)	8.1210(7)	
cell parameter c (Å)	7.4728(7)	13.8207(1)
cell parameter γ (deg)	112.974(8)	

[a] The reliability factors R_P, R_{WP}, R_I, and R_F are the profile factor, weighted profile factor, Bragg factor, and crystallographic factor, respectively.

Figure 4a shows the time evolution of the particle sizes for the samples prepared at different temperatures. The particle size clearly increases with reaction temperature from 160 to 250 °C, whereas 350 °C appears to have slightly slower growth rate and reach smaller particle sizes than 250 °C. The growth rate also increases from 160 to 250 °C presumably mainly due to the enhancement of the specific interface energy and grain boundary mobility at high temperatures. The formation becomes much quicker when the reaction temperature is increased as indicated by the scale factors shown in Figure 4b. The formation of $BiFeO_3$ crystals finishes within seconds at 350 °C. This is seen from the scale factor, which directly reaches a maximum once the $BiFeO_3$ phase can be detected.

Another point worthy of mention is the lattice parameters of the $BiFeO_3$ nanoparticles which deviate from bulk materials when the particle size decreases to a certain value. Selbach et al.[22] have described the rhombohedral structure of $BiFeO_3$ as a pseudotetragonal structure using normalized lattice parameters $a_N = a/\sqrt{2}$ and $c_N = c/\sqrt{12}$. c_N/a_N is larger than unity for bulk $BiFeO_3$. c_N/a_N becomes equal to unity for an ideal cubic perovskite. They reported a phenomenon that the lattice parameters of $BiFeO_3$ deviate from bulk materials with a_N increasing and c_N decreasing as a function of particle size below 30 nm,

dx.doi.org/10.1021/cm102575w |*Chem. Mater.* 2011, 23, 1158–1165

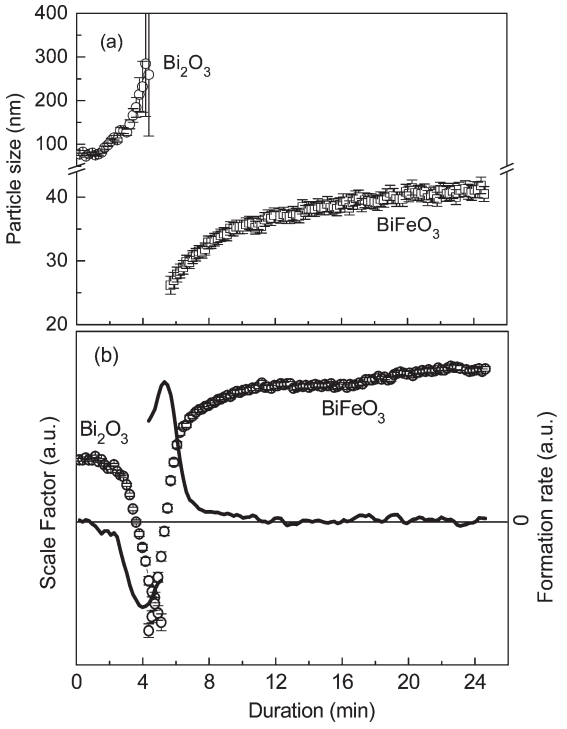

Figure 3. Time evolutions of (a) particle sizes, (b) scale factors (open circle), and formation rates (solid line) of Bi_2O_3 and $BiFeO_3$ for sample IS200.

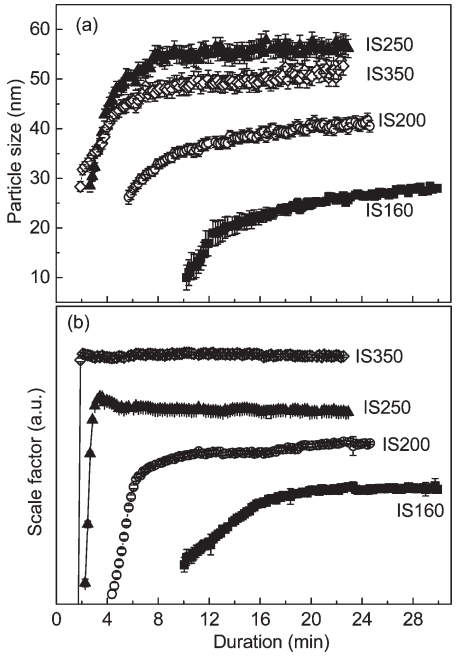

Figure 4. Time evolution of (a) particle sizes and (b) scale factors for the different samples IS160, IS200, IS250, and IS350. The scale factors are normalized and an offset is used between each curve.

indicating a tendency toward cubic symmetry with decreasing grain size. Here, we have converted the lattice parameters a and c obtained from the Rietveld refinements to normalized lattice parameters of our in situ data. The time evolution of normalized lattice parameters $a_N = a/\sqrt{2}$ and $c_N = c/\sqrt{12}$ together with the

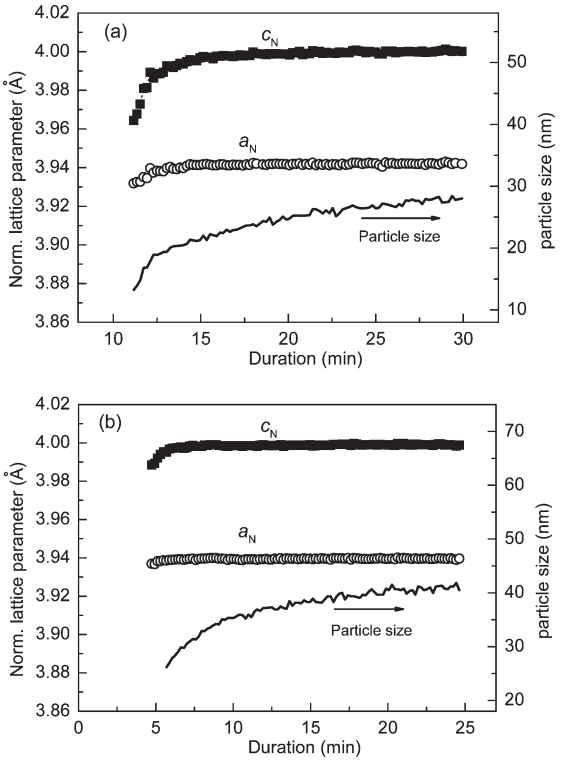

Figure 5. Time evolutions of normalized lattice parameters a_N (open circle), c_N (solid square), and particle sizes (solid line) of samples IS160 (a) and IS200 (b).

particle sizes of samples IS160 and IS200 are shown in Figure 5. After 15 min of reaction, the lattice parameters a_N = 3.94 and c_N = 4.00 of sample IS160 are in good agreement with bulk materials. The c_N deviates from the bulk value when the reaction time is below 15 min and decreases with decreasing reaction time, corresponding to the decrease in particle size from 20 to 10 nm. However, a_N does not significantly deviate from the bulk for short reaction time or small particle size, which is not the same as Selbach et al.'s result. In any case, both the results indicate that the rhombohedral structure of $BiFeO_3$ approaches a cubic perovskite structure with decreasing particle size, corresponding to the normalized lattice parameters becoming equal. A similar phenomenon is also found in IS200 as shown in Figure 5b; however, the phenomenon is not obvious in IS250 or in IS350 due to their relative large particle sizes (see the Supporting Information).

3.2. Structure and Phase Study of $BiFeO_3$ Nanoparticles. The PXRD patterns of sample BFO_SC and BFO_H prepared by supercritical synthesis and hydrothermal route, respectively, are shown in Figure 6. BFO_H is found to be pure $BiFeO_3$, while a $Bi_{25}FeO_{40}$ impurity is detected in sample BFO_SC, possibly due to the short reaction time during the continuous flow supercritical synthesis. The crystal sizes of the samples were determined by the Scherrer equation through fitting the peaks by a Lorentz function. A silicon standard was used to account for the instrumental broadening. The crystallite size calculated from [101] is about 40(2) nm for BFO_SC. The calculated crystallite size of BFO_H is about 90(4) nm, which approaches the limit for reliable estimates, and the average crystallite size of BFO_H possibly is larger than 90 nm. Figure 7 shows the typical morphologies of the two samples. BFO_SC is mostly composed

dx.doi.org/10.1021/cm102575w |*Chem. Mater.* 2011, 23, 1158–1165

of fine particles with particle size below 20 nm. Some large particles with particle sizes of about 100 nm are observed. From the SEM image of sample BFO_H, the sample is heavily aggregated and the particles are up to micrometers in size. However, sample BFO_H should be polycrystalline, so the actual crystallite size is smaller corresponding to the average value of about 90 nm.

Differential scanning calorimetry shown in Figure 8 reveals that the DSC curve of BFO_H has four endothermic peaks at 543, 1101, 1189, and 1208 K. The endothermal effect starting at 543 K and showing a broad feature lasting until 793 K could be the onset of magnetic ordering. The Néel transition temperature for bulk materials is reported to be at around 643 K.[6] A broadening of the transition was also observed by Mazumder et al.[23] According to the most complete study of the phase diagram of $BiFeO_3$,[6,24] there are three distinct solid phases from room temperature to the melting point: the ferroelectric α phase (rhombohedral) below the Curie temperature, an intermediate β phase (orthorhombic) in the region 1103−1198 K, and a cubic γ phase before decomposition and subsequent melting, which are in good agreement with our DSC study of sample BFO_H shown the inset of Figure 8. The peak of 1101 K can be interpreted as α−β transition, which is the ferroelectric−paraelectric transformation, and in good agreement with the reported value of 1098 K of $BiFeO_3$ single crystals.[6] An intermediate phase transition 30 K below the transition to the β phase has been observed by some authors;[6,24] however, this is absent in our data. Around 1189 K, there is a weak $\beta-\gamma$ transition from the orthorhombic phase to a high symmetry cubic $Pm\bar{3}m$ phase. Since $BiFeO_3$ is very unstable at the high temperature $\beta-\gamma$ transition and it rapidly decomposes into other phases, it seems that not all measurements can detect the cubic phase at high temperature.[24] This is the case for the BFO_SC data shown in Figure 8. The endothermal peak at 1208 K of sample BFO_H is the peritectic decomposition of the cubic phase into the melt and $Bi_2Fe_4O_9$. Only the α−β transition at 1103 K and the peritectic decomposition at 1233 K were detected in the DSC curve of sample BFO_SC. The absence of other peaks presumably is because the endothermic effects are too weak to be detected for sample BFO_SC.

Detailed knowledge of the symmetry, lattice parameters, and atomic positions of the ferroelectric and antiferromagnetic $BiFeO_3$ phase (α phase) is required to understand the relationships between structure and properties. Multitemperature SR-PXRD of BFO_H was investigated from 100 to 1000 K to study the temperature dependence of the α phase which is rhombohedral and belongs to the space group *R*3*c*. Figure 9 shows a refined

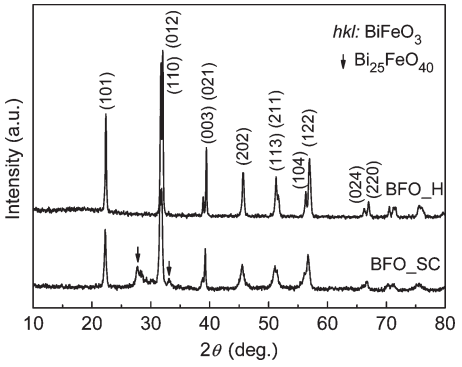

Figure 6. XRD patterns of BFO_SC and BFO_H prepared by supercritical synthesis and hydrothermal route, respectively.

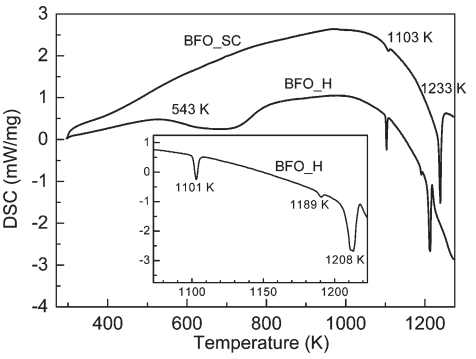

Figure 8. DSC curves for sample BFO_H and BFO_SC at temperatures between room temperature to 1273 K. The inset is a zoom in on the DSC curve for BFO_H at high temperatures.

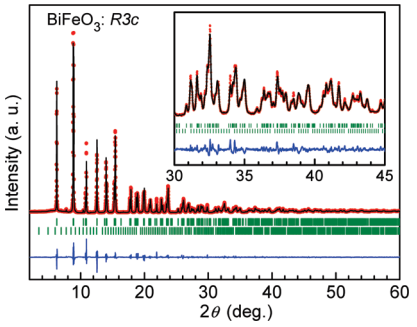

Figure 9. Observed and calculated diffraction patterns and the difference profile at 100 K of sample BFO_H. An impurity of $Bi_{25}FeO_{39}$ is identified with a concentration of 0.45%. The inset shows the detailed features at higher 2θ angles.

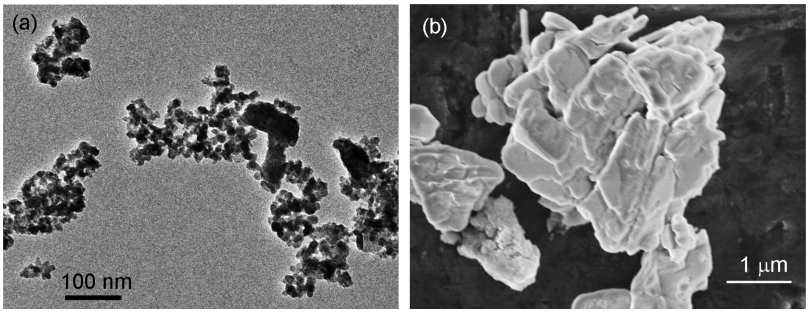

Figure 7. (a) TEM image of BFO_SC prepared by supercritical synthesis and (b) SEM image of BFO_H prepared by hydrothermal synthesis.

dx.doi.org/10.1021/cm102575w |*Chem. Mater.* 2011, 23, 1158–1165

powder diffraction pattern of the 100 K data with the observed, calculated, and difference patterns. The inset shows the detailed features observed at higher angles. A trace of impurity $Bi_{25}FeO_{39}$ with space group of $I23$[25] is identified in the powder diffraction pattern. The concentration of $Bi_{25}FeO_{39}$ in the sample is only about 0.45% at 100 K and does not change significantly in the measured temperature range. The refined parameters and crystallographic details from the Rietveld analysis of the synchrotron powder diffraction data for 100, 300, and 1000 K are given in the Supporting Information.

Figure 10 shows the temperature dependences of the lattice parameters of sample BFO_H in the hexagonal system description. A slight offset between the data measured at low and high temperature is due to small systematic errors between the two experimental setups. Bucci et al.[26] reported a Néel temperature of 598−617 K by investigating the temperature dependences of lattice parameters. The transition is not visible in our results due to the insufficient temperature resolution with a step size of 100 K in the SR-PXRD data, which is too large to detect the Néel temperature. A simple Einstein function is often used to model the thermal expansion.[27] Here, the temperature dependence of the lattice parameter a is modeled with the Einstein equation:

$$\ln\left(\frac{a}{a_0}\right) = A \times \frac{\theta}{e^{(\theta/T)} - 1} \qquad (2)$$

where a_0 is the lattice parameter at T = 0 K, θ is the phonon energy, and A is a scaling coefficient. The solid line of lattice parameter a shown in Figure 10 is the Einstein mode fit with a phonon energy θ of 929(95) K, a_0 = 5.5721(8) Å, and A = 0.000010(1). Similarly, the lattice parameter c below 800 K can be modeled with Einstein mode with a phonon energy θ' of 478(96) K, c_0 = 13.835(3) Å, and A' = 0.000010(1). However, the lattice parameter c deviates from the Einstein model above 800 K. The thermal expansion along c decreases above 800 K, indicating that the high temperature structure is approaching the phase transition.

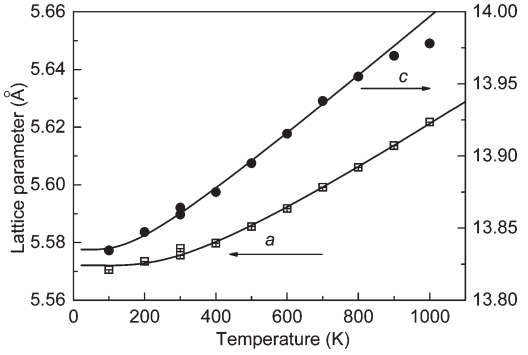

Figure 10. Temperature dependences of the lattice parameters for sample BFO_H in the hexagonal system description. The solid lines are the Einstein model fits.

3.3. Magnetic Properties of $BiFeO_3$ Nanocrystals. To characterize the magnetic properties of the $BiFeO_3$ nanocrystals, magnetic measurements were performed on both the hydrothermal and supercritical synthesized samples. Figure 11a,b shows the $M-H$ hysteresis loops at 300 and 10 K for BFO_H and BFO_SC, respectively. The $M-H$ hysteresis loops at 300 K reported by Park et al.[28] for bulk $BiFeO_3$ and for 41 nm nanocrystals are also shown in Figure 11a for comparison. Both

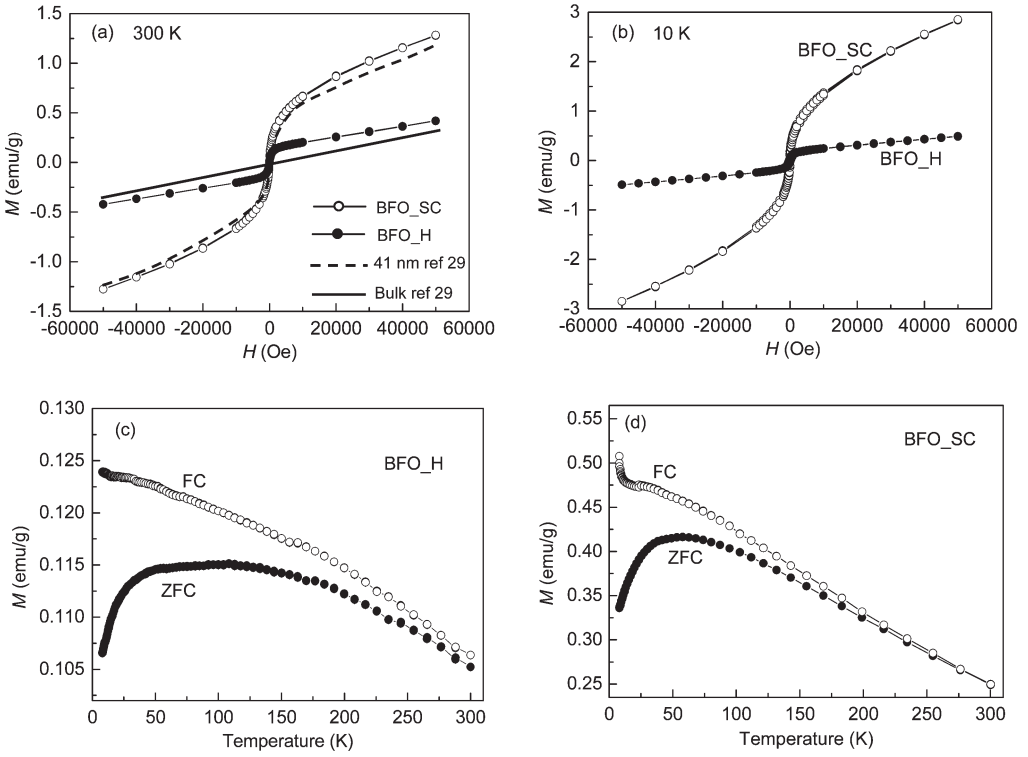

Figure 11. (a) Hysteresis loops at 300 K for BFO_H and BFO_SC together with those of bulk $BiFeO_3$ and 41 nm nanocrystals (ref 29), (b) hysteresis loops at 10 K for BFO_H and BFO_SC. (c, d) Temperature dependences of the magnetization under 1000 Oe in zero field cooling (ZFC) and field cooling (FC) mode.

dx.doi.org/10.1021/cm102575w |*Chem. Mater.* 2011, 23, 1158–1165

BFO_H and BFO_SC show magnetic response and display strong size-dependent magnetic behavior. The $M-H$ curves for bulk $BiFeO_3$ at 300 K change linearly with the magnetic field, and the spontaneous magnetization is very small. This is typical for antiferromagnetic arrangement of the Fe^{3+} magnetic moments. On the other hand, the nanocrystals of $BiFeO_3$ show enhanced magnetization and superparamagnetism correlated with decreasing diameter. Both BFO_H and BFO_SC show distinct nonlinearity in the $M-H$ curves. The room temperature magnetization values for BFO_H and BFO_SC are 0.42 and 1.23 emu/g at a field of 50 kOe, respectively. The magnetic hysteresis loops of BFO_SC with an estimated average size of 40 nm are in good agreement with 41 nm sized crystals reported by Park et al. Here a magnetization value of 0.34 emu/g was reported for bulk $BiFeO_3$ and 1.22 emu/g for 41 nm $BiFeO_3$ nanocrystals at room temperature and a field of 50 kOe. It has been reported that bulk polycrystalline $BiFeO_3$ shows a linear $M-H$ loop with absence of coercivity both at 300 and 10 K.[29] Compared with our $BiFeO_3$ nanocrystals, no obvious coercivities are detected for both BFO_H and BFO_SC at 300 K. However, when the measuring temperature is 10 K, the nonlinear $M-H$ loops are accompanied by coercivities (see the Supporting Information). The distinct size effects of the magnetic properties in $BiFeO_3$ nanocrystals are due to the large fraction of uncompensated spins on the surfaces of the nanocrystals or the result of uncompensated magnetic moments originating from canting of the otherwise antiferromagnetically aligned magnetic moments of the Fe^{3+} ions. Furthermore, the magnetic structure of bulk $BiFeO_3$ has been shown to be a G-type antiferromagnetic structure with a weak canting of the moments. The finite moments result from the canting order in a 62−64 nm spirally modulated superstructure.[30] The superstructure will be affected by particle size, and the coercivities observed in nanosized $BiFeO_3$ might be related to the breaking of this super structure. However, the presence of impurities in the samples could also affect the magnetic properties.

Figure 11c,d shows the ZFC and FC magnetizations versus temperature curves under 1000 Oe for sample BFO_H and BFO_SC, respectively. Large differences between the ZFC and FC curves are detected which are quite similar to observations on bulk single crystals, for which the differences were attributed to spin-glasslike behavior.[24,31] Similar effects were observed by Jaiswal et al. for $BiFeO_3$ nanoparticles, and the difference between the ZFC and FC magnetization curves was shown to decrease with increasing particle size.[29] It was proposed that the broad peak in the ZFC curves is related to the breaking of the above-described 62 nm spiral modulation of the G-type antiferromagnetic ordering. However, a recent study of single crystalline $BiFeO_3$ did not show any difference between the ZFC and the FC magnetization curves, and it was concluded that the previously observed differences were due to impurity phases in samples of limited quality.[32] The lack of any transitions below room temperature to other phases or spin glass states was further supported by heat capacity measurements. The contradictory results in the literature therefore prevent a definitive interpretation of the low temperature magnetization measurements performed in this study.

4. CONCLUSION

The formation and growth of $BiFeO_3$ nanocrystals in high-temperature, high-pressure aqueous solution is studied by in situ synchrotron radiation powder X-ray diffraction, and phase pure $BiFeO_3$ was obtained. Synthesis in high-temperature, high-pressure conditions is a rapid method for the preparation of $BiFeO_3$ nanocrystals. The formation of $BiFeO_3$ possibly involves the combination of crystalline bismuth oxide and amorphous ferric hydroxide. The lattice parameters of $BiFeO_3$ deviate from the bulk materials when the particle size is below 20 nm, indicating a tendency toward cubic symmetry with decreasing crystallite size. $BiFeO_3$ nanocrystals were successfully prepared in an autoclave and in a continuous flow supercritical system, respectively. The Néel transition is broad and ranging over ∼200 K due to the reduced crystal sizes. Both samples showed nanosize effects in the magnetic properties and enhanced magnetization correlated with decreasing particle size. The magnetic measurements at 10 K reveal a weak ferromagnetic behavior where the magnetization has clear coercivity. A surface spin disorder could be responsible for the property due to the increase of the number of uncompensated spins associated with Fe^{3+} ions in $BiFeO_3$ nanocrystals. However, the presence of impurities in the samples may affect the magnetic properties.

■ ASSOCIATED CONTENT

Supporting Information. The time evolutions of SR-PXRD patterns for the samples IS160, IS250, and IS350, time evolutions of normalized lattice parameters a_N and c_N, and particle sizes of samples IS250 and IS350, temperature dependences of Bi−O and Fe−O bond distances for sample BFO-H, zoom views of the hysteresis loops for BFO_H and BFO_SC, and refined parameters and crystallographic details from the Rietveld analysis of BFO_H (PDF). This material is available free of charge via the Internet at http://pubs.acs.org.

■ AUTHOR INFORMATION

Corresponding Author
*E-mail: bo@chem.au.dk.

■ ACKNOWLEDGMENT

This work was supported by the Danish National Research Foundation (Center for Materials Crystallography), the Danish Strategic Research Council (Center for Energy Materials), and the Danish Research Council for Nature and Universe (Danscatt). MAX-lab is thanked for the beamtime. Kirsten Ø. Jensen and Jacob Becker are thanked for assistance during the in situ experiments. Peter Hald is thanked for the help in continuous flow supercritical synthesis. The synchrotron radiation experiment at the SPring-8 synchrotron was conducted with the approval of the Japan Synchrotron Radiation Research Institute.

■ REFERENCES

(1) Wang, J.; Neaton, J. B.; Zheng, H.; Nagarajan, V.; Ogale, S. B.; Liu, B.; Viehland, D.; Vaithyanathan, V.; Schlom, D. G.; Waghmare, U. V.; Spaldin, N. A.; Rabe, K. M.; Wuttig, M.; Ramesh, R. *Science* **2003**, *299*, 1719–1722.
(2) Eerenstein, W; Mathur, N. D.; Scott, J. F. *Nature* **2006**, *442*, 759–765.
(3) Choi, T.; Choi, Y. J.; Kiryukhin, V.; Cheong, S.-W. *Science* **2009**, *324*, 63–66.
(4) Fiebig, M.; Lottermoser, T.; Fröhlich, D.; Goltsev, A. V.; Pisarev, R. V. *Nature* **2002**, *419*, 818–820.
(5) Tokura, Y. *Science* **2006**, *312*, 1481–1482.

(6) Palai, R.; Katiyar, R. S.; Schmid, H.; Tissot, P.; Clark, S. J.; Robertson, J.; Redfern, S. A. T.; Catalan, G.; Scott, J. F. *Phys. Rev. B* **2008**, *77*, 014110.
(7) Li, S.; Lin, Y.-H.; Zhang, B.-P.; Wang, Y.; Nan, C.-W. *J. Phys. Chem. C* **2010**, *114*, 2903–2908.
(8) Chen, C.; Cheng, J.; Yu, S.; Che, L.; Meng, Z. *J. Cryst. Growth* **2006**, *291*, 135–139.
(9) Basu, S.; Pal, M.; Chakravorty, D. *J. Magn. Magn. Mater.* **2008**, *320*, 3361–3365.
(10) Cho, C. M.; Noh, J. H.; Cho, I.-S.; An, J.-S.; Hong, K. S.; Kim, J. Y. *J. Am. Ceram. Soc.* **2008**, *91*, 3753–3755.
(11) Hald, P.; Becker, J.; Bremholm, M.; Pedersen, J. S.; Chevallier, J.; Iversen, S. B.; Iversen, B. B. *J. Solid State Chem.* **2006**, *179*, 2674–2680.
(12) Hald, P.; Bremholm, M.; Ibersen, S. B.; Iversen, B. B. *J. Solid State Chem.* **2008**, *181*, 2681–2683.
(13) Byrappa, K.; Ohara, S.; Adschiri, T. *Adv. Drug Delivery Rev.* **2008**, *60*, 299–327.
(14) Jensen, H.; Bremholm, M.; Nielsen, R. P.; Joensen, K. D; Pedersen, J. S.; Birkedal, H.; Chen, Y.-S.; Almer, J.; Søgaard, E. G.; Iversen, S. B.; Iversen, B. B. *Angew. Chem., Int. Ed.* **2007**, *46*, 1113–1116.
(15) Bremholm, M.; Jensen, H.; Iversen, S. B.; Iversen, B. B. *J. Supercrit. Fluids* **2008**, *44*, 385–390.
(16) Bremholm, M.; Becker-Christensen, J.; Iversen, B. B. *Adv. Mater.* **2009**, *21*, 3572–3575.
(17) Tyrsted, C.; Becker, J.; Hald, P.; Bremholm, M.; Pedersen, J. S.; Chevallier, J.; Cerenius, Y.; Iversen, S. B.; Iversen, B. B. *Chem. Mater.* **2010**, *22*, 1814–1820.
(18) Bremholm, M.; Felicissimo, M. P.; Iversen, B. B. *Angew Chem., Int. Ed.* **2009**, *48*, 4788–4791.
(19) Becker, J.; Bremholm, M.; Tyrsted, C.; Pauw, B.; Jensen, K. M. Ø.; Eltzholt, J.; Christensen, M.; Iversen, B. B. *J. Appl. Crystyallogr.* **2010**, *43*, 729–736.
(20) Rodríguez-Carvajal, J. *FULLPROF, A profile refinement program*; ILL: France, 2007.
(21) Nishibori, E.; Takata, M.; Kato, K.; Sakata, M.; Kubota, Y.; Aoyagi, S.; Kuroiwa, Y.; Yamakata, M.; Ikeda, N. *Nucl. Instrum. Methods Phys. Res., Sect. A* **2001**, *467*, 1045–1048.
(22) Selbach, S. M.; Tybell, T.; Einarsrud, M.-A.; Grande, T. *Chem. Mater.* **2007**, *19*, 6478–6484.
(23) Mazumder, R.; Ghosh, S.; Mondal, P.; Bhattacharya, D.; Dasgupta, S.; Das, N.; Sen, A.; Tyagi, A. K.; Sivakumarb, M.; Takami, T.; Ikuta, H. *J. Appl. Phys.* **2006**, *100*, 033908.
(24) Catalan, G.; Scott, J. F. *Adv. Mater.* **2009**, *21*, 2463–2485.
(25) Radaev, S. F.; Muradyan, L. A.; Simonov, V. I. *Acta Crystallogr.* **1991**, *B47*, 1–6.
(26) Bucci, J. D.; Robertson, B. K.; James, W. J. *J. Appl. Crystallogr.* **1972**, *5*, 187–191.
(27) Jorgensen, J. D.; Hinks, D. G.; Short, S. *Phys. Rev. B* **2001**, *63*, 224522.
(28) Park, T.-J.; Papaefthymiou, G. C.; Viescas, A. J.; Moodenbaugh, A. R.; Wong, S. S. *Nano Lett.* **2007**, *7*, 766–772.
(29) Jaiswal, A.; Das, R.; Vivekanand, K.; Abraham, P. M.; Adyanthaya, S.; Poddar, P. *J. Phys. Chem. C* **2010**, *114*, 2108–2115.
(30) Sosnovska, I.; Peterlin-Neumaier, T.; Steichele, E. *J. Phys. C: Solid State Phys.* **1982**, *15*, 4835–4846.
(31) Singh, M. K.; Prellier, W.; Singh, M. P.; Katiyar, R. S.; Scott, J. F. *Phys. Rev. B* **2008**, *77*, 144403.
(32) Lu, J.; Günther, A.; Schrettle, F.; Mayr, F.; Krohns, S.; Lunkenheimer, P.; Pimenov, A.; Travkin, V. D.; Mukhin, A. A.; Loidl, A. *Eur. Phys. J. B* **2010**, *75*, 451–460.